The Effect of Chromium on the Weldability and Microstructure of Fe-Cr-Al Weld Cladding

The composition range of weldable alloys is identified along with the potential beneficial role of carbides

BY J. R. REGINA, J. N. DUPONT, AND A. R. MARDER

ABSTRACT. Iron-aluminum-based weld cladding is currently being considered as corrosion-resistant coatings for boiler tubes in coal-fired power plants. Although these alloys could potentially be good coating candidates due to their excellent high-temperature corrosion resistance, Fe-Al weld cladding is susceptible to cracking due to hydrogen embrittlement at elevated aluminum concentrations. Additions of chromium to these iron-aluminum alloys have been shown to improve the corrosion resistance of the alloys and could potentially increase the lifetimes of the coatings. The current study investigated the effect of chromium on the hydrogen cracking susceptibility of Fe-Al weld cladding. The results showed that chromium and aluminum are uniformly distributed in the cladding on both a macroscopic and microscopic scale. The uniform microscopic distribution is attributed to the high diffusion rates of chromium and aluminum in ferrite. The cracking susceptibility of these alloys is a strong function of the aluminum and chromium content of weld cladding. Additions of chromium to Fe-Al weld cladding will decrease the amount of aluminum that can be accommodated in the cladding before cracking occurs. The hydrogen cracking susceptibility of the welds was not linked exclusively to the formation of the inherently brittle intermetallic compounds (Fe_3Al and FeAl) as observed from previous results on Fe-Al weld cladding. The presence of $(Fe,Cr)_xC_y$ and $(Fe,Al)_3C$ type carbides was found to improve the cracking resistance of the cladding to the point where crack-free welds could be obtained on some of the cladding that contained the brittle intermetallic phases. This improvement in cracking resistance is attributed to the hydrogen trapping potential of the carbide phases. Conversely, cracking was occasionally observed in high chromium/low aluminum alloys that did not exhibit any of the intermetallic phases. It is suggested that cracking in these alloys may be associated with reaction of chromium and aluminum with water vapor in the arc that liberates free hydrogen.

Introduction

Iron-chromium-aluminum-based alloys are good candidates for corrosion-resistant weld cladding because they exhibit excellent oxidation and sulfidation resistance in a wide range of high-temperature environments. These alloys rely on both aluminum and chromium additions for increased corrosion protection, and it has been shown that the corrosion resistance of these alloys in simulated low NOx environments improved with an increase in the aluminum and chromium concentrations[1]. Recent studies have indicated that Fe-Cr-Al-based alloys require approximately 7.5–10 wt-% aluminum and chromium additions up to ~ 5 wt-% to remain protective in a wide variety of low NOx-type atmospheres (Refs. 1, 2). Unfortunately, work to date has shown that weld cladding that contains the brittle

FeAl and/or Fe_3Al intermetallics are susceptible to cracking due to environmental embrittlement.

Liu (Ref. 3) was one of the first investigators to demonstrate that premature cracking of FeAl and Fe_3Al intermetallics is due to hydrogen embrittlement. In that work, the room-temperature ductility of FeAl and Fe_3Al intermetallic alloys was investigated under carefully controlled environments. The FeAl and Fe_3Al alloys each exhibited significant ductility (~12% elongation) when tensile tested under high-vacuum or pure oxygen environments (i.e., with no water vapor). The introduction of water vapor into the test chamber decreased the ductility significantly down to 2–4%. Hydrogen embrittlement of the intermetallic phases has been attributed to their general lack of ductility coupled with the generation of hydrogen that occurs when aluminum reacts with water vapor to liberate free hydrogen via the reaction $2Al + 3H_2O \rightarrow Al_2O_3 + 6H^+ + 6e^-$.

While many theories for hydrogen embrittlement exist, the presence of hydrogen in these alloys is expected to cause embrittlement by significantly lowering the cleavage strength (Ref. 4). This type of mechanism is also believed to be responsible for cracking observed in Fe-Al cladding that contains the intermetallic phases in which Al reacts with water vapor in the arc to liberate hydrogen. This, coupled with residual stresses from welding, can cause cracking in Fe-Al cladding that contains the FeAl and Fe_3Al phases. For example, it has previously been reported that Fe-Al cladding produced with both the GTAW and GMAW processes were

---

J. R. REGINA, formerly a graduate student, is currently group leader of Welding and Fabrication at ExxonMobil, Houston, Tex. J. N. DUPONT is professor, Materials Science and Engineering, and associate director, Energy Research Center; and A. R. MARDER is emeritus professor, Materials Science and Engineering, Lehigh University, Bethlehem, Pa.

1. *In this article, the nomenclature Fe-Al or Fe-Cr-Al is used to denote Fe-based alloys with additions of Cr and/or Al without specific regard to the type of phases that form, while the FeAl and Fe_3Al nomenclature is used to identify the corresponding ordered intermetallics that can form in this alloy system at specific composition ranges.*
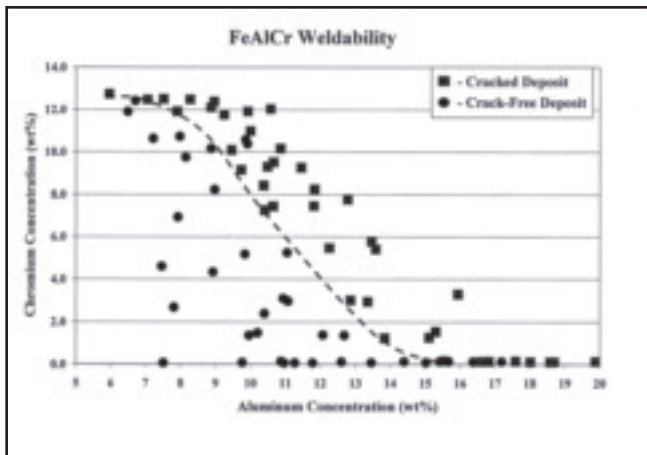
Fig. 1 — Cracking susceptibility of the weld cladding as a function of aluminum and chromium concentration.

subject to this cracking phenomenon when the aluminum concentration in the weld deposit was greater than approximately 8–11%Al (Ref. 5), and this Al range represents the composition over which the intermetallics begin to form in the cladding. Cracks that formed on welds were observed to penetrate through the thickness of the fusion zone where they stopped at the base metal. This type of cracking would provide direct paths through the corrosion-resistant weld coatings, and thus allow corrosive gas species to attack the underlying substrate. Weld cladding containing these types of cracks would essentially provide no corrosion protection at cracked areas and would be unacceptable for these applications.

Other work (Refs. 6, 7) has shown that the use of a minimum 350°C preheat temperature combined with postweld heat treating at a minimum of 750°C can be used to alleviate the cracking in the weld cladding. Experiments conducted under a controlled welding chamber has also shown that reduction of the water vapor content helps eliminate the cracking. However, these remedies are not practical for most applications in which a relatively large amount of surface area must be clad for corrosion protection under industrial processing conditions. In these applications, the most practical route to avoiding the problem is to identify weld compositions that are resistant to cracking under processing conditions that utilize typical shielding gases and no preheat or postweld heat treatment.

In view of this, the influence of Cr on the weldability of Fe-Al alloys warrants further consideration. McKamey et al. (Ref. 8) have shown that the ductility of alloys exhibiting the intermetallic phases can be improved significantly with Cr additions, while more recent work (Refs. 9, 10) has shown that Cr is also beneficial to corrosion resistance. Therefore, the objective of this study is to determine the ef-

fect of Cr on the weld cladding microstructure and corresponding cracking susceptibility of Fe-Al weld cladding under practical processing conditions without the use of preheat or postweld heat treatment. The results of this work forms the basis for identifying Fe-Cr-Al cladding compositions that can be used as corrosion-resistant coatings.

Experimental Procedure

Single-pass gas tungsten arc (GTA) weld cladding was deposited onto 4 × 12 × ¼ in. (102 × 305 × 6.4 mm) A285C carbon steel using a dual wire feeder system with commercially pure 1100 aluminum and 430 ferritic stainless steel filler metals. A smaller matrix of welds was prepared on a low-carbon experimental substrate. The chemical compositions of the steel substrates and the filler metals are shown in Table 1. Welds with a wide range of aluminum and chromium concentrations were prepared by independently varying the feed rates of the two filler metal wires. The plate surfaces were ground using a SiC grinding wheel to remove any scale and to expose bare metal. The weld deposits were produced using a constant current power source at a fixed current of 220 A. The voltage was controlled at approximately 11 V by maintaining a constant arc length between the tungsten electrode (~4 mm diameter) and the substrate. An argon shielding gas was used with a reported moisture content of less than approximately 300 ppm. It should be noted that the Al filler metal
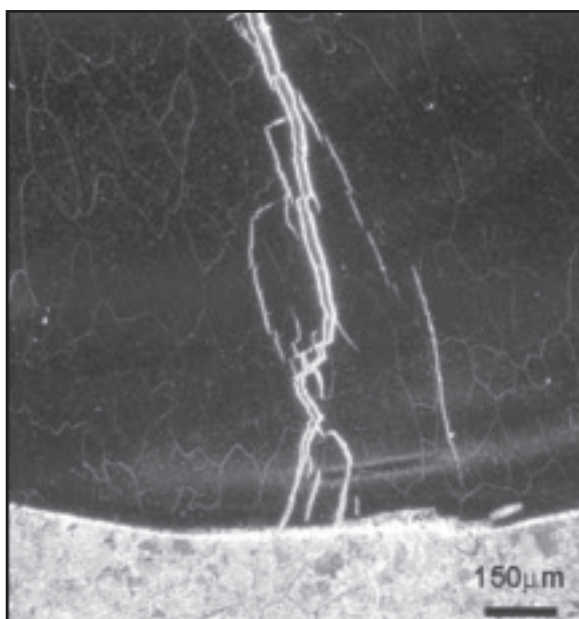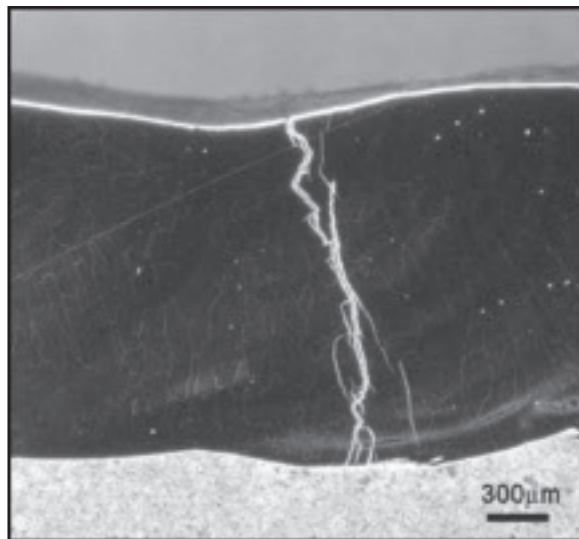

Fig. 2 — LOM photomicrographs showing examples of typical cracks observed in the cladding.

may also provide a source of hydrogen as it may be covered with a hydrated oxide. Welds approximately 8 in. (~200 mm) long were produced with a travel speed of 2 mm/s, and welds were therefore produced at an energy input of approximately 1210 J/mm. The filler metal feed speeds were then independently varied from 0 to 74 mm/s to adjust the aluminum and chromium contents of the weld deposits.

The cracking behavior of the weld deposits was investigated using a nondestructive dye penetration technique. Welds were allowed to cool and were left for at least 48 hours before testing for cracks. This was done to ensure sufficient time for cracking to occur, as welds susceptible to hydrogen cracking can require an incubation period before cracks form within the weld (Refs. 11, 12). Weld
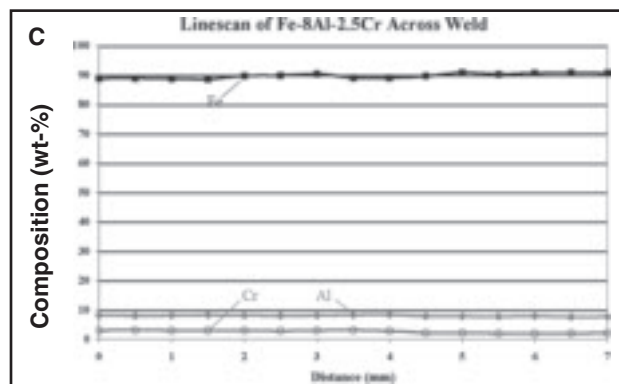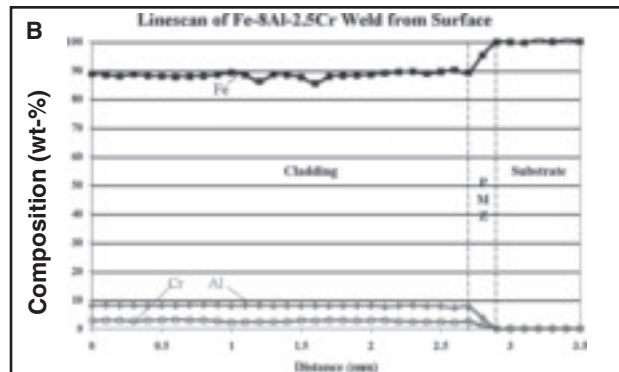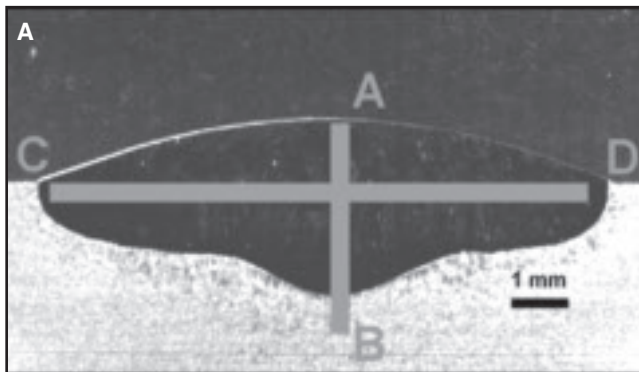
Fig. 3 — A — LOM photomicrograph showing location of EPMA traces on a Fe-2.7Cr-7.8Al weld; B — EPMA trace acquired from the weld surface to the substrate; C — EPMA trace acquired across the width of the weld.

cladding compositions were determined using electron probe microanalysis (EPMA) by taking several large-area scans within the fusion zone of the weld (2–3 cm). Potential macrosegregation in the welds was investigated with EPMA by measuring the chemical composition at points spaced between 0.1 and 0.5 mm apart. Potential microsegregation of alloying elements was investigated by measuring the chemical composition across the width of grains at 2-µm intervals. All EPMA data were collected at an accelerating voltage of 20 keV and a current of 50 nA. A phi (ρz) correction scheme was used to correct for any absorption and fluorescence of x-ray that occurs during EPMA collection.

Phase identification was conducted using x-ray diffraction (XRD) on a Bruker AXS general area detector diffraction system using Co Kα x-rays (λ = 1.78897 nm) over a 2Θ range of approximately 30–100 deg for times up to 2 h. Samples for XRD were ground with SiC paper to a 600-grit finish and cleaned with acetone. Weld samples were removed in cross section, mounted, and polished to a 0.01-µm SiO_2 finish for light optical microscopy (LOM). Samples were etched in a 4% picral solution containing a few drops of HCl for 3–40 min. Measurements of the particle area fraction and number of particles per unit area of weld were made using a LECO© quantitative image analysis (QIA) system interfaced with a light optical microscope. Area fraction measurements were assumed to be equivalent to volume fraction (Ref. 13). Scanning electron microscopy (SEM) was used to obtain images of larger carbide particles at an accelerating voltage of 5 keV. Energy-dispersive spectroscopy (EDS) was used to determine the chemical makeup of the larger carbides and was taken using voltages from 5 to 15 keV and a collection live time of approximately 100 s.

Identification of fine-scale carbides was performed by removing the carbide precipitates from the matrix using a carbide extraction technique (Ref. 14). Weld cladding samples were first etched in the 4% picral solution containing approximately 5% HCl to reveal the carbide microstructure. A microstructural replica was then produced by placing a drop of methyl acetate onto the etched sample and depositing a small square of cellulose acetate film onto the weld metal surface. The methyl acetate allowed for the cellulose acetate to soften enough to penetrate into the microstructural features of the weld metal. A capillary reaction between the cellulose acetate and the weld metal resulted in the extraction of carbides present in the weld fusion zone. The cellulose acetate film was then coated with a thick layer of carbon using an evaporation chamber, ensuring that the carbon coat was applied to the side of the film that contained the particles from the weld metal. The film was then submerged into a methyl acetate bath to allow the cellulose acetate to dissolve away, leaving behind small carbon films suspended within the solution. Copper grids were used to "catch" the carbon films floating in the methyl acetate solution, and they were transferred to an isopropyl alcohol bath to remove the methyl acetate. Another copper grid was used to remove the carbon film from the isopropyl alcohol, and it was left to dry on a mesh platinum drying rack. The copper grids containing the carbon film and carbides from the weld metal were loaded into the transmission electron microscope (TEM) for analysis. Bright-field TEM images were taken at 120 keV on a JEOL 420 TEM. Energy-dispersive spectroscopy (EDS) was also performed on carbides using an accelerating voltage of 120 keV and a collection live-time of 60 s.

Table 1 — Chemical Compositions of Filler Metals and Substrates Used in Welding Tests (wt-%)

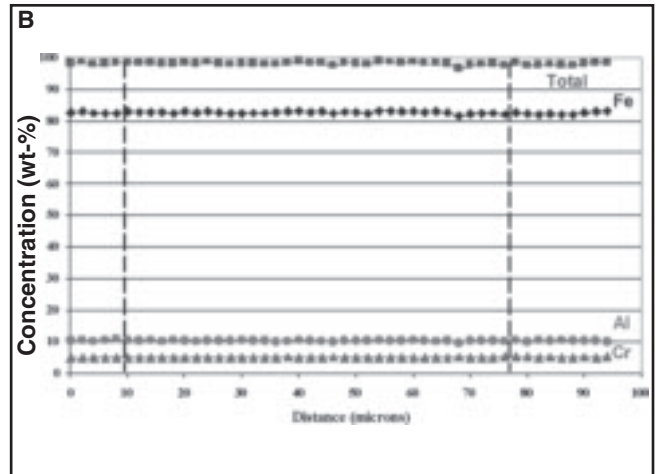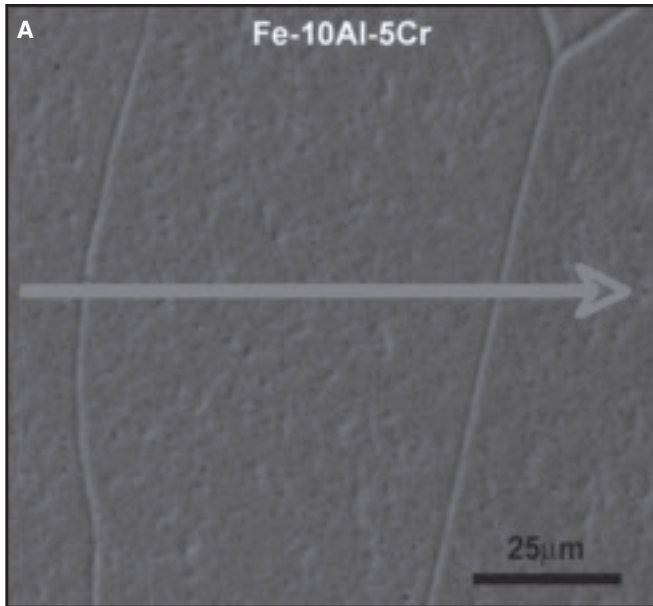| Element	Al Filler Metal	Fe-Cr Filler Metal	A285 Grade C Steel Substrate	Low C Steel Substrate
Fe	0.12	Balance	Balance	Balance
Al	Balance	<0.001	0.031	<0.005
Cr	0.011	16.63	0.086	<0.01
C	0.006	0.029	0.16	0.017
P	0.073	0.020	0.005	0.003
S	0.001	0.003	0.001	0.003
Mn	0.011	0.32	0.52	<0.01
Cu	0.13	0.089	0.284	0.002
Ni	0.009	0.20	0.148	0.02
Mo	0.003	0.034	0.055	<0.002
Ti	0.013	<0.001	0.019	0.002
Si	0.36	0.33	0.043	<0.01

Fig. 4 — A — LOM photomicrograph showing location of EMPA trace conducted across a grain in a Fe-5.3Cr-11.0Al weld; B — EPMA trace acquired across the grain.
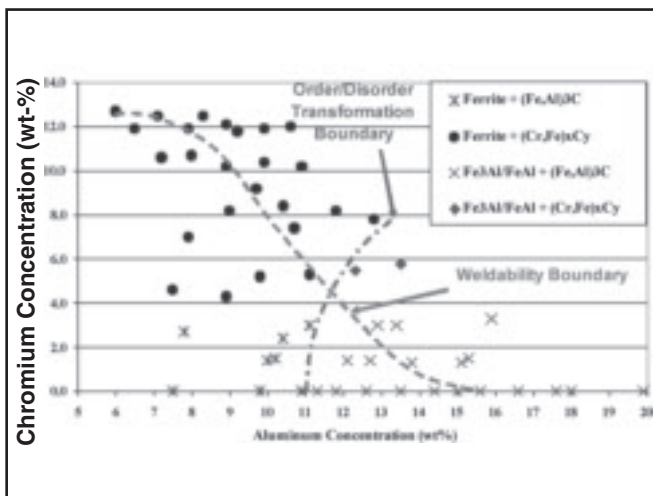

Fig. 5 — X-ray diffraction phase identification results of the cladding. The weldability boundary from Fig. 1 is superimposed on the results.
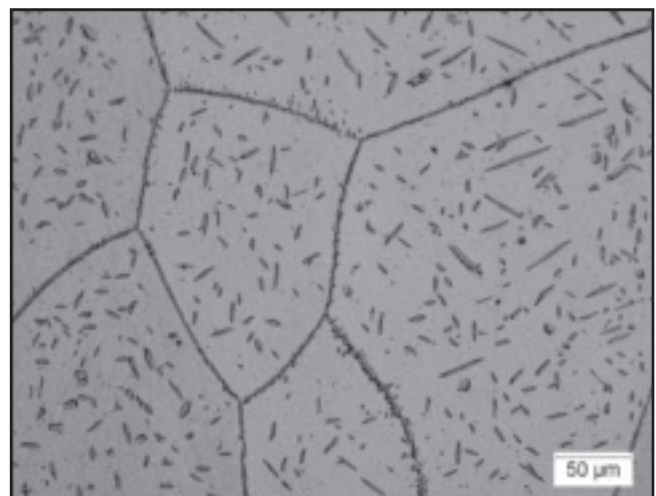

Fig. 6 — LOM photomicrograph of the $(Fe,Al)_3C$ carbides that were observed in welds with less than ~4 wt-% chromium.

Results and Discussion

Cracking Susceptibility and Microstructural Characterization

Figure 1 shows the cracking susceptibility of the weld cladding as a function of aluminum and chromium concentration. The binary Fe-Al welds were deposited crack-free up to approximately 15 wt-% Al. Additions of chromium into the weld decreased the amount of aluminum that could be accommodated before cracking occurred. A typical example of the cracks observed in the cladding is shown in Fig. 2. All the cracks were predominately transgranular with some small amount of intergranular cracking, and this morphology is consistent with hydrogen cracking of these alloys observed in other research (Refs. 5,

15). Corrosion results of previous studies reported that Fe-Cr-Al alloys required approximately 7.5–10% Al and chromium additions up to approximately 5 wt-% Cr to provide adequate corrosion protection in simulated low NOx corrosion environments (Refs. 1, 2). The weldability results shown in Fig. 1 indicate crack-free cladding should be obtainable with these composition ranges under the current set of processing conditions.

A typical transverse cross section of the Fe-2.7Cr-7.8Al (all values are in wt-%) weld cladding and the EPMA traces performed on this sample can be seen in Fig. 3. EPMA traces taken from the weld surface into the underlying substrate showed that the weld compositions remained constant through the fusion zone until the partially mixed zone (PMZ), where there

was a transition from the weld cladding composition to the substrate composition. The partially mixed zones present in the cladding were on the order of approximately 200 μm and did not significantly deviate with the welding parameters. EPMA traces performed across the width of the weld fusion zones showed that the weld cladding compositions remained constant through the width of the coatings. These results indicate there was good mixing between the two filler metal wires and the substrate during weld deposition.

Microscopic segregation of alloying elements was investigated by performing EPMA traces across entire weld grains at 2-μm intervals. Typical results for weld cladding samples containing intermediate aluminum and chromium levels (Fe-5.3Cr-11.0Al) are shown in Fig. 4. These

results show that the aluminum and chromium concentrations are also evenly distributed throughout the fusion zone on a microscopic scale. Reference to the Fe-Cr-Al ternary liquidus projection (Ref. 16) indicates that all the weld compositions investigated in this study will solidify as ferrite. The lack of any microsegregation in the weld cladding can be attributed to this primary solidification mode.

It is well known that the diffusion rates of chromium and aluminum are relatively high in ferrite when compared to austenite (Ref. 17). Thus, any solute redistribution that occurs during solidification can be homogenized during postsolidification cooling by back diffusion, which accounts for the uniform distribution of aluminum and chromium shown in Fig. 4.

As a result, these Fe-Cr-Al coatings should not experience any preferential corrosion when exposed to low NOx environments, which is typical of Ni-based and stainless steel alloys that experience microsegregation during welding (Ref. 18). Problems with corrosion-fatigue cracking in Ni-based alloys have been related to localized preferential attack of the dendrite cores where the alloying elements needed for corrosion protection are low due to microsegregation. Because the critical alloying elements required for corrosion protection in Fe-Cr-Al weld cladding are homogeneously distributed, they should demonstrate improved resistance to this form of corrosion-fatigue cracking.

The XRD phase identification results are shown in Fig. 5. There were four microstructural regimes observed in the weld cladding: ferrite with $(Fe,Al)_3C$ carbides, ferrite with $(Cr,Fe)_xC_y$ carbides, $Fe_3Al/FeAl$ with $(Fe,Al)_3C$ carbides, and $Fe_3Al/FeAl$ with $(Cr,Fe)_xC_y$ carbides. The weldability boundary from Fig. 1 is superimposed on the phase ID results for reference, and the approximate location of the order/disorder transformation boundary that indicates the formation of $Fe_3Al/FeAl$ intermetallic phases is also shown. It was not possible to distinguish between the Fe_3Al and FeAl intermetallic phases, so they are collectively grouped as $Fe_3Al/FeAl$ here. The phase fields containing $Fe_3Al/FeAl$ phases may have also contained ferrite, but due to the peak overlap between these phases, it could only be determined that the intermetallic phases were present within the weld metal as a result of the super lattice reflections. Thus, the order/disorder transformation boundary describes the composition range where ferrite phase begins to transform to the ordered intermetallic phases. Iron and chromium rich carbides, such as Fe_3C, $M_{23}C_6$, and M_7C_3 (where M typically represents a combination of Fe, Cr, and Mo) were identified by comparing these low-intensity XRD peaks with the reported powder diffraction files for these mixed iron-chromium carbides (Ref. 19). Because there was very little molybdenum present within the filler metal wires and the steel substrates, it was unlikely that these carbides contained any significant amount of Mo. Because both types of carbides were observed in the weld samples and the actual compositions of these carbides within the welds were unknown, these types of carbides were collectively referred to as $(Cr,Fe)_xC_y$.

The phase identification results show that the intermetallic phases began to form at aluminum concentrations of approximately 11% in the binary Fe-Al weld cladding, which is in agreement with the phases present within the Fe-Al phase diagram (Ref. 20). Chromium additions appeared to moderately stabilize the ferrite phase, as increasing the chromium content of the weld caused the intermetallic transformation to occur at higher aluminum concentrations. According to the binary Fe-Al phase diagram, a two-phase region of ferrite + Fe_3Al has been reported to exist between approximately 11 wt-% Al and 13 wt-% Al. From the reported phase diagrams, the actual order/disorder transformation may have occurred over a range of aluminum concentrations, where the onset of the ordered transformation began at approximately 11 wt-% Al and may not have completely transformed to the ordered intermetallic Fe_3Al phase until approximately 13 wt-% Al (for binary Fe-Al welds). The $(Fe,Al)_3C$ carbides form in the weld cladding containing less than 4 wt-% Cr, whereas welds containing above approximately 4 wt-% Cr contained the $(Cr,Fe)_xC_y$-type carbides. The role of composition and microstructure on the cracking susceptibility of these alloys is discussed in more detail below.

Figure 6 shows an LOM photomicrograph of the $(Fe,Al)_3C$ carbides that were observed in welds with less than ~ 4 wt-% chromium. The carbides exhibited an
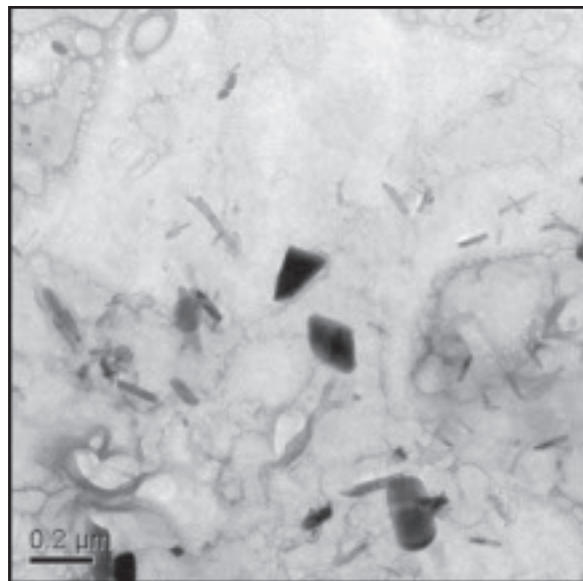

Fig. 7 — Typical TEM image of the carbides observed in the welds that had chromium contents greater than 4 wt-%.
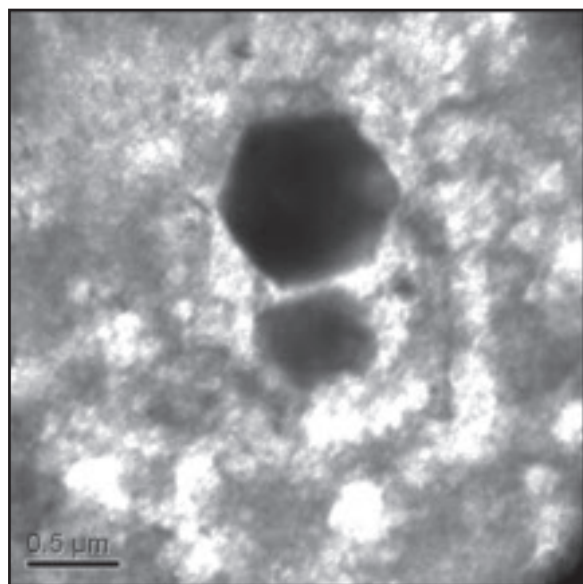

Fig. 8 — TEM photomicrograph showing examples of large hexagonally shaped particles were observed in all the weld cladding.

elongated, needle-like morphology and were present at grain boundaries and within the grains. EDS analysis of these carbides confirmed that they contained only Fe, Al, and C. Figure 7 shows a typical TEM image of the carbides observed in the welds that had chromium contents greater than 4 wt-%. These welds exhibited two types of carbide morphologies — one with a block-like appearance that was on the order of ~ 150–300 nm in size, and smaller elongated carbides that were generally less than 200 nm long and 50 nm wide. EDS analysis indicated that both types of carbides contained only iron and chromium. These results support the
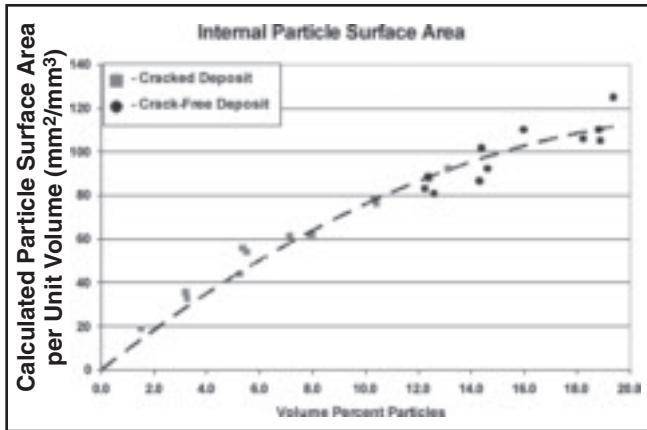
Fig. 9 — Calculated particle surface area per unit volume of weld metal as a function of volume percent particles for welds containing the (Fe, Cr)$_x$C$_y$-type carbides.
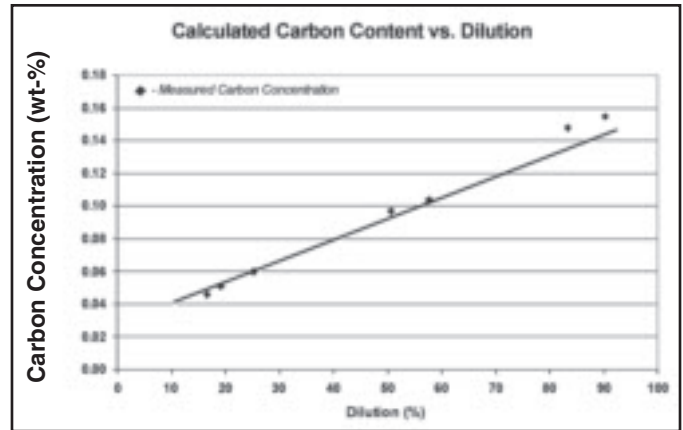

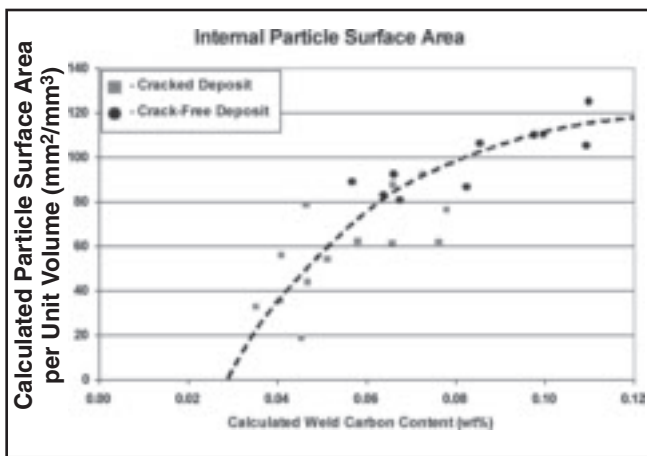Fig. 10 — Weld metal carbon concentrations as a function of dilution.

Fig. 11 — Calculated particle surface area as a function of weld metal carbon concentration for welds containing the (Fe, Cr)$_x$C$_y$-type carbides.

XRD results, which indicated that M$_{23}$C$_6$ and M$_7$C$_3$ carbides were present in the weld cladding containing greater than 4 wt-% Cr. As shown in Fig. 8, large hexagonal-shaped particles were also observed. These particles were present in all the weld cladding, regardless of the coating composition, and typically ranged in size from approximately 400 nm to larger than 1 μm in diameter. EDS analysis revealed that these particles were rich in aluminum, but did not contain chromium or iron. These Al-rich particles were most likely Al$_2$O$_3$ particles that formed during deposition of the weld cladding due to the reaction between the liquid aluminum and water vapor present within the weld atmosphere (Ref. 21). Although these particles were large in size, there was a relatively low amount of these particles compared to the amount of carbides within the weld, and this accounts for their inability to be detected by XRD.

The potential formation of martensite in the cladding warrants consideration for two reasons. First, martensite can form in alloys that enter the austenite (γ) phase field on cooling. The Fe-Cr and Fe-Al binary systems each exhibit a γ "loop." The γ loop in the Fe-Cr system exists from 0 to ~ 13 wt-% Cr, while it exists from 0 to ~ 2 wt-% Al in the Fe Al system (Ref. 22). Second, the martensite phase is also well known to be susceptible to cracking during welding under the presence of hydrogen (e.g., Ref. 11). Phase equilibria in the Fe-Cr-Al ternary system has been well established and ternary phase diagrams are available from the liquidus projection down to 450°C for this system (Ref. 23). Inspection of those diagrams shows that, in the ternary Fe-Cr-Al system, the primary solidification phase is ferrite (α) under all the compositions considered in this study. In addition, the ferrite phase is stable at all lower temperatures for Al concentrations greater than ~ 2 wt-%, regardless of the Cr content. This covers the entire range of compositions investigated here. The α → γ transformation only occurs during cooling under a relatively small composition space for alloys with less than 13 wt-% Cr and 2 wt-% Al. This indicates that the Al level in the weld cladding considered in this study (> 6 wt-% Al) is high enough to stabilize the ferrite phase at all temperatures, thus eliminating possible formation of martensite. This is confirmed by the metallographic examinations and phase identification results. Thus, cracking in these alloys cannot be attributed to martensite formation.

Influence of Second-Phase Particles on Cracking Susceptibility

Research conducted to date has shown that the hydrogen cracking susceptibility of Fe-Al-type alloys is linked exclusively to the presence of the brittle Fe$_3$Al and FeAl intermetallic phases (Refs. 5, 15). However, the combined weldability and phase ID results shown in Fig. 5 indicate that the cracking susceptibility of these weld claddings cannot be linked solely to the presence of the intermetallic phases. Crack-free welds could be deposited on some compositions that exhibited the intermetallic phases, while cracking was observed on some of the alloys that did not exhibit any of the ordered intermetallic phases. These results indicate that the addition of chromium and the presence of second-phase particles has a strong influence on the cracking susceptibility of these alloys.

Recent research has demonstrated particles such as carbides, oxides, and nitrides can act as hydrogen trapping sites (Refs. 24–28). Permanent hydrogen trapping sites can reduce the overall amount of diffusible hydrogen available to embrittle the metal, and can therefore reduce the cracking susceptibility of the alloy (Ref. 29). The effectiveness of microstructural features to trap hydrogen depends largely on the type of feature. For example, oxide inclusions are more effective trapping sites than dislocations, while carbides are even more effective than oxides at trapping free hydrogen (Refs. 25, 26, 30). A study investigating hydrogen-assisted cracking of 1¼Cr-1Mo steel has reported that mixed iron, chromium, and molybdenum carbides such as M$_{23}$C$_6$ and M$_7$C$_3$ are effective hydrogen trapping sites (Ref. 31). These results indicate that the
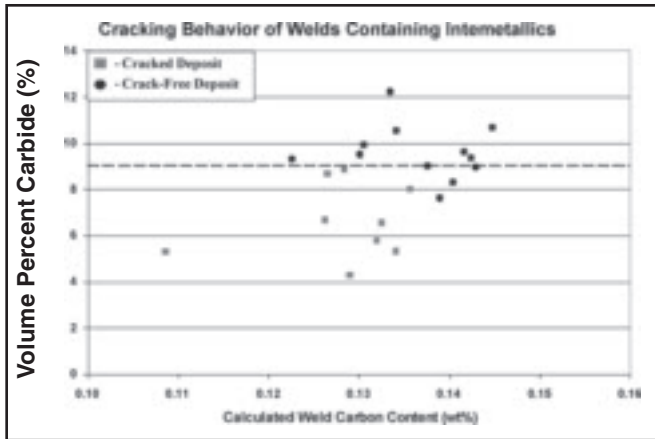
Fig. 12 — Influence of carbide content on the cracking susceptibility of welds containing the $(Fe,Al)_3C$-type carbides.
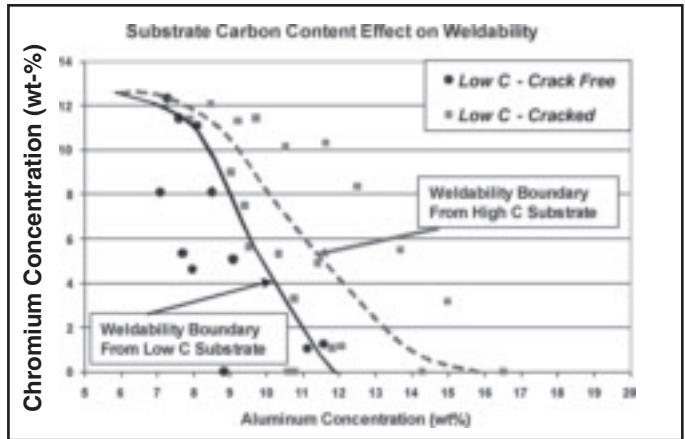

Fig. 13 — Cracking results of welds made on the low-carbon substrate. The weldability limit from welds made on the higher carbon substrate are also shown for reference.

presence of these types of carbides ($M_{23}C_6$ and M_7C_3) may have a beneficial effect on the hydrogen cracking susceptibility by reducing the amount of diffusible hydrogen within the weld metal. Other studies have shown that Al_2O_3 particles can also act as effective hydrogen trapping sites and reduce the susceptibility of steels to hydrogen embrittlement (Ref. 32). In view of these factors, the quantity of second-phase particles was considered in more detail in an effort to understand their influence on the cracking behavior of these alloys.

Weld Cladding Containing $(Cr,Fe)_xC_y$ Type Carbides

The volume fraction and number of particles per unit area of weld of $(Cr,Fe)_xC_y$ and Al_2O_3 particles was determined using quantitative image analysis for the welds that contained the $(Cr,Fe)_xC_y$-type carbides. These measurements included both carbides and oxide particles because the two microstructural features could not be accurately separated on a quantitative basis and because previous results reported that both types of particles can potentially act as effective permanent hydrogen trapping sites (Refs. 31, 32). Although the size and number of particles within the welds are expected to effect the amount of trapped hydrogen, the amount of particle surface area within the weld should provide a more direct indication on the effectiveness of the particles to trap hydrogen. This is based on the idea that hydrogen trapping sites rely on the segregation of hydrogen to the particle/matrix interface, rather than hydrogen incorporation into the actual carbide or oxide (Refs. 29, 33–35). The amount of particle surface area per unit volume of weld (PSA) is related to the volume fraction (f_v) and number of particles

per unit area (N_A) by (Ref. 36)

$$PSA = 3\sqrt{\pi}\sqrt{(f_v N_A)} \quad (1)$$

Use of this relation between f_v, N_A, and PSA to determine the effectiveness of these particles as trapping sites is only semiquantitative due to the following assumptions: 1) the carbides and oxides are equally effective hydrogen trapping sites, 2) the carbides and oxides were spherical in nature, and 3) there was no particle clustering within the metal.

Figure 9 shows that the particle surface area per unit volume of weld metal increases as the volume percent of particles increases, which is expected. More importantly, the results indicate that the cracked and crack-free welds can be separated based on their particle surface area. For the current welding conditions, welds containing particle/matrix interfacial areas less than approximately 80 mm²/mm³ were susceptible to hydrogen cracking. Welds containing between approximately 80 mm²/mm³ and 100 mm²/mm³ particle surface area values appeared to undergo a transition between cracked and crack-free welds. Weld cladding containing particle surface areas greater than approximately 100 mm²/mm³ was found to be immune to hydrogen cracking. This correlation between the amount of particle surface area and the susceptibility of the welds to hydrogen cracking indicates that the size and distribution of particles within the weld has a significant effect on the hydrogen cracking behavior of the Fe-Cr-Al weld cladding. It should be noted that the amount of PSA required to prevent cracking is expected to depend on the particle type, amount of hydrogen available, and residual stress. Thus, the results presented here are not intended to provide a general value of PSA required to prevent cracking,

but to demonstrate the important role of particles in reducing the cracking susceptibility of these alloys.

The primary source of carbon (and associated carbide formation) in the claddings comes from the substrate, which contained approximately 0.16 wt-%C. By comparison, the Fe-Cr and Al filler metals contained only 0.029 wt-%C and 0.006 wt-%C, respectively. Low-dilution welds obtained by high filler metal feed rates exhibit high chromium and aluminum concentrations, but low-carbon concentrations. Thus, the amount of carbides observed in the weld deposits was observed to increase with increasing dilution level (due to increased carbon from the base metal). This can be shown in more detail by considering the quantitative relations between dilution and weld metal carbon content.

The concentration of element i in the weld metal varies with dilution by

$$C_w^i = C_{bm}^i D + C_{fm}^i (1 - D) \quad (2)$$

where D is the dilution, C_w^i is concentration of element i in weld metal, C_{bm}^i is the concentration of element i in base metal, and C_{fm}^i is the concentration of element i in filler metal. When two filler metals are used, an equation is needed for the effective filler metal composition fed into the weld pool. The effective filler metal composition is simply given by a law of mixtures type expression as

$$C_{fm}^i {}^* = \left(\frac{\rho_{Al} V_{Al}}{\rho_{Al} V_{Al} + \rho_{FeCr} V_{FeCr}} \right) C_{Al}^i + \left(\frac{\rho_{FeCr} V_{FeCr}}{\rho_{Al} V_{Al} + \rho_{FeCr} V_{FeCr}} \right) C_{FeCr}^i \quad (3)$$

where $C_{fm}^i{}^*$ is the effective concentration of element i in the "effective filler metal,"

C^i_{Al} is the concentration of element i in the Al wire, C^i_{FeCr} is the concentration of element i in the Fe-Cr wire, V_{Al} is the volumetric feed rate for the Al wire, and V_{FeCr} is the volumetric feed rate for Fe-Cr wire. ρ_{Al} is the density of the Al wire, and ρ_{FeCr} is the density of the Fe-Cr wire. The volumetric feed rate for each filler metal wire depends on the wire diameter and the linear feed rate for each wire

$$V_{Al} = \left(\frac{\pi}{4}\right)(d_{Al})^2 \upsilon_{Al} \quad (4a)$$

$$V_{FeCr} = \left(\frac{\pi}{4}\right)(d_{FeCr})^2 \upsilon_{FeCr} \quad (4b)$$

where d_{Al} is the diameter of Al wire, d_{FeCr} is the diameter of Fe-Cr wire, υ_{Al} is the linear feed rate for Al wire, and υ_{FeCr} is the linear feed rate for Fe-Cr wire. Once the effective filler metal concentration is known, the dilution for each Fe-Cr-Al weld cladding can be calculated by rearranging Equation 2

$$D = \frac{C^i_w - C^i_{fm}{}^*}{C^i_{bm} - C^i_{fm}{}^*} \quad (5)$$

Using the calculated dilution values for each weld sample, the carbon concentration could then be calculated knowing the base metal and filler metal carbon concentrations

$$C^c_w = C^c_{bm}D + C^c_{fm}{}^*(1-D) \quad (6)$$

where C^c_w is the weld metal carbon concentration, C^c_{bm} is the base metal carbon concentration, and $C^c_{fm}{}^*$ is the effective filler metal carbon concentration.

The calculated carbon concentrations for the Fe-Cr-Al weld cladding are shown as a function of dilution in Fig. 10. Direct measurements of carbon contents made on several welds using wet chemical analysis techniques are also shown in the figure, and these measured carbon contents are in good agreement with the carbon contents calculated from dilution measurements. These results demonstrate that the carbon concentration is expected to increase with increasing dilution. The corresponding relation between particle surface area, carbon content, and associated cracking susceptibility is shown in Fig. 11. As expected, the particle surface area generally increases with an increase in weld carbon content, which can be attributed to increased formation of $(Cr,Fe)_xC_y$ type carbides. This plot also shows that, for the current welding conditions, approximately 0.08 wt-%C is required to prevent hydrogen cracking in cladding containing greater than 4 wt-%Cr.

Weld Cladding Containing (Fe,Al)₃C-Type Carbides
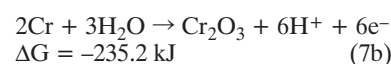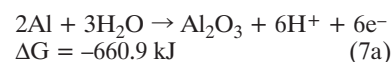
Accurate estimations of the particle surface area of the $(Fe,Al)_3C$ carbides could not be made because the particles were elongated and could not be approximated as spherical. However, as shown in Fig. 12, a general trend was still observed in which crack-free welds could be made above a certain volume percent of $(Fe,Al)_3C$ carbides, which is ~ 9 volume percent for the current conditions. These measurements were made only on welds that contained both the $(Fe,Al)_3C$ carbides and the intermetallic phases. Welds comprised of the ferrite phase and $(Fe,Al)_3C$ carbides were excluded from this analysis because these welds were immune to hydrogen cracking regardless of the presence of $(Fe,Al)_3C$ carbides. There is no simple relation between carbon content and carbide volume percent for these welds. Although this relation was not investigated in detail, it may be related to formation of Al_2O_3 that competes with formation of the $(Fe,Al)_3C$ carbide.

Weld Cladding on Low-Carbon Substrates

The results described above suggest that the carbon content of the weld should influence the amount of carbides in the weld and the corresponding resistance to hydrogen cracking. In general, welds made on higher carbon substrates should form more carbides and therefore be more resistant to hydrogen cracking. The cracking results of welds made on the low-carbon substrates shown in Fig. 13 conform to this expected trend. The weldability limit for the high-carbon substrate is provided with these results for comparison. There is a rather distinct compositional boundary between welds that were cracked and crack-free for each substrate. These results show that a reduction in carbon content associated with the lower carbon substrate significantly decreases the range of weldable compositions. The difference in cracking behavior between the low- and high-carbon welds is most significant at the lower chromium levels where the intermetallic phases form. Volume fraction measurements made on select samples confirmed that the amount of carbides in welds made on the low-carbon substrate was much lower than those made on the high-carbon substrate. For example, a 10.2Al-5.3Cr cladding made on the low-carbon substrate contained only ~1 vol-% of particles and cracked, whereas a 9.8Al-5.2Cr cladding (i.e, similar aluminum and chromium levels) deposited on the higher carbon steel plate contained ~15 vol-% particles and was deposited crack-free.

The cracking observed in the higher chromium welds with ferrite and $(Cr,Fe)_xC_y$ carbides warrants some discus-sion. Up to this point, hydrogen embrittlement of these alloys has been linked to the formation of the Fe_3Al and FeAl intermetallic phases. However, the results obtained here show that cracking can also occur in the ferrite phase. Cracking in the intermetallic phases has been attributed to their general lack of ductility coupled with the generation of hydrogen that occurs when aluminum reacts with water vapor in the arc to liberate free hydrogen. It should be noted that chromium can also react with water vapor in a similar manner to form free hydrogen. The corresponding reactions and Gibbs free energies of formation at approximately 1500°C for each case are given by (Ref. 37)

$$2Al + 3H_2O \rightarrow Al_2O_3 + 6H^+ + 6e^-$$
$$\Delta G = -660.9 \text{ kJ} \quad (7a)$$

$$2Cr + 3H_2O \rightarrow Cr_2O_3 + 6H^+ + 6e^-$$
$$\Delta G = -235.2 \text{ kJ} \quad (7b)$$

The large, negative energies of formation suggest that reaction of both aluminum and chromium with water vapor are expected. If this reaction between chromium and water vapor were to occur along with the reaction between aluminum and water vapor, the amount of hydrogen incorporated into the weld metal could significantly increase. Also note that the higher chromium welds are made at low dilution levels where carbon pickup into the weld from the substrate will be low, resulting in only a small amount of carbides that may be insufficient to resist cracking.

These factors may account for the cracking observed in the high-chromium ferritic weld cladding, although more work is needed to confirm this. Fully ferritic welds may also possess low ductility due to large grain size. However, the grain size of the weld cladding was generally ≤ 300 μm, which would not be expected to cause a significant loss in ductility. In addition, all the welds exhibited similar grain sizes (which is expected since they were all prepared under similar processing conditions), but exhibited a range of cracking behavior. Thus, the cracking susceptibility of the higher chromium welds with ferrite and $(Cr,Fe)_xC_y$ carbides is not expected to be linked to the grain size.

Conclusions

The weldability and microstructure of Fe-Cr-Al weld cladding deposited onto carbon steel substrates was investigated. The following conclusions can be drawn from this research:

1) Chromium and aluminum are uniformly distributed in these weld cladding on both a macroscopic and microscopic scale. The uniform macroscopic distribution is attributed to good mixing between

the filler metals and substrate, while the uniform microscopic distribution is attributed to the high diffusion rates of chromium and aluminum in ferrite.

2) The cracking susceptibility of these alloys is a strong function of the aluminum and chromium content of the cladding. Additions of chromium to the Fe-Al weld cladding will decrease the amount of aluminum that can be accommodated before cracking begins to occur in the cladding.

3) The hydrogen cracking susceptibility of the Fe-Cr-Al welds cannot be linked exclusively to the formation of the inherently brittle intermetallic compounds (Fe_3Al and $FeAl$). The presence of $(Cr,Fe)_xC_y$ and $(Fe,Al)_3C$ carbides significantly affected the cracking behavior of welds, as high amounts of these carbides prevented hydrogen cracking in samples containing the intermetallic compounds.

4) Cracking observed in high-chromium/low-aluminum welds that did not contain any ordered phase appears to be associated with evolution of free hydrogen due to reaction between chromium and aluminum with water vapor combined with a small amount of carbides available that were insufficient to resist cracking, but more work is needed to confirm this possible mechanism.

References

1. Regina, J. R., DuPont, J. N., and Marder, A. R. 2004. Gaseous corrosion resistance of Fe-Al based alloys containing Cr additions. Part I — kinetic results. Accepted for Publication, *Mat. Sci. and Eng.*, A.

2. Regina, J. R., DuPont, J. N., and Marder, A. R. 2004. Corrosion behavior of Fe-Al-Cr alloys in sulfur- and oxygen-rich environments in the presence of pyrite. *Corrosion* 60, pp. 501–509.

3. Liu, C. T., Lee, E. H., and McKamey, C. G. 1989. An envrionmental effect as the major cause for room-temperature embrittlement if iron-aluminum. *Scripta Metallurgica*, 23, pp. 875–880.

4. Mendiratta, M. G., Ehlers, S. K., Chatterjee, D. K., and Lipsitt, H. A. 1987. Tensile flow and fracture behavior of DO3 iron-25 at-% aluminum and iron-31 at-% aluminum alloys. *Metallurgical and Materials Transactions* A, 18A, pp. 283–291.

5. Banovic, S. W., DuPont, J. N., Tortorelli, P. F., and Marder, A. R. 1999. The role of aluminum on the weldability and sulfidation behavior of iron-aluminum cladding. *Welding Journal* 78: 23-s to 30-s.

6. Doodwin, G. M. 1997. Weld overlay cladding with iron aluminides. *Proceedings of the 11th Annual Fossil Energy Materials Conference*, Knoxsville, Tenn. published by Department of Energy, pp. 217–224.

7. Santella, M. L. 1996. An overview of the welding of Ni_3Al and Fe_3Al alloys. *Proceedings of the International Symposium on Nickel and Iron Aluminides*, Dayton, Ohio, pp. 321–327, ASM International, Materials Park, Ohio.

8. McKamey, C. G., Horton, J. A., and Liu, C. T. 1989. Effect of chromium on properties of iron aluminide. *Journal of Materials Research*, 4, pp. 1156–1163.

9. Regina, J. R., DuPont, J. N., and Marder, A. R. 2005. Gaseous corrosion resistance of Fe-Al-based alloys containing Cr additions Part I: Kinetic results. *Materials Science and Engineering* A. 404(1-2): 71–78.

10. Regina, J. R., DuPont, J. N., and Marder, A. R. 2005. Gaseous corrosion resistance of Fe-Al based alloys containing Cr additions Part II. Scale morphology. *Materials Science and Engineering* A. 405(1-2): 102–110.

11. Kou, S. 2003. *Welding Metallurgy*, Wiley-Interscience, New York, N.Y.

12. Hertzberg, R. W. 1996. *Deformation and Fracture Mechanics of Engineering Materials,* John Wiley & Sons, Inc., New York, N.Y.

13. ASTM, *Standard Test Method for Determining Volume Fraction by Systematic Manual Point Count*. 1992. Annual Book of ASTM Standards, 03.01 edition, pp. 99–110. American Society for Testing Materials.

14. Marder, A. R., Wilkins, J. C., Maniar, G. N., Nail, D. A., and Robinson, D. L. 1973. Extraction replica techniques. *Manual on Electron Metallography Techniques.* Ed. by G. N. Maniar and A. Szirmae, pp. 19–28. ASTM, American Society for Testing and Materials, Philadelphia, Pa.

15. Liu, C. T., McKamey, C. G., and Lee, E. H. 1990. Environmental effects on room-temperature ductility and fracture in iron aluminide (Fe_3Al). *Scripta Metallurgica et Materialia* 24, 385–389.

16. Grunert, A., Hesselbruch, W., and Schistal, K. 1935. On the high heat-resistant Cr-Al-Fe alloys with and without cobalt. *Electrowaerme* 5, pp. 131–132.

17. Smithells, C. J. 1992. *Smithells Metals Reference Book*, Butterworth and Heinemann, Oxford, England.

18. Luer, K. 2000. Corrosion fatigue of alloy 625 weld cladding exposed to combustion environments. *Adv. Mater. Processes* 157: 24–25.

19. Powder Diffraction File Database. JCPDS - International Center for Diffraction Data. [2.1], 01-1262 (Fe). 50-0955 (Fe_3Al). 33-0020 (FeAl). 89-3193 ($AlFe_3C$). 35-0783 ($Cr_{23}C_6$). 36-1482 (Cr_7C_3). 03-0989 (Fe_3C). 2000.

20. Kattner, U. R. 1990. Fe-Al equilibrium phase diagram. *Binary Alloy Phase Diagrams,* 2nd Ed., ed. by T. Massalski, pp. 147–149. ASM International, Metals Park, Ohio.

21. Speidel, M. O. 1977. Hydrogen embrittlement of aluminum alloys. *Hydrogen Damage* Ed. by C. D. Beachem, pp. 329–351. American Society for Metals, Metals Park, Ohio.

22. *ASM Handbook*, 1992. Vol. 3, Alloy phase diagrams, Ed. Hugh Baker, ASM International, Materials Park, Ohio, pp. 2-44 and 2-152.

23. *Ternary Alloys – A Comprehensive Compendium of Evaluated Constituional Data and Phase Diagrams*, Vol. 4, 1991. Ed. G. Petzow and G. Effenberg, ASM International, Materials Park, Ohio, pp. 329–341.

24. Podgurski, H. H., and Oriani, R. A. 1972. Nitrogenation of Fe-Al alloys. Pt. 3 absorption of H in nitrogenated Fe-Al alloys. *Metall. Trans.* 3, pp. 2055–2063.

25. Lee, J. L., and Lee, J. Y. 1986. The interaction of hydrogen with the interface of Al_2O_3 particles in Iron. *Metall. Mater. Trans.* A 17A, pp. 2183–2186.

26. Asaoka, T., Dagbert, C., Aucouturier, M., and Galland, J. 1977. Quantitative study of trapping characteristics of H in a Fe-0.15% Ti ferrite by high-resolution autoradiography and during degassing at high temperatures. *Scr. Metall.* 11, pp. 467–472.

27. Lee, H. G., and Lee, J. Y. 1984. Hydrogen Trapping by TiC Particles in Iron. Acta Met. 32, pp. 131–136.

28. Pressouyre, G. M., and Bernstein, I. M. 1978. A quantitative analysis of hydrogen trapping. *Metall. Mater. Trans.* A 9A, pp. 1571–1580.

29. Maroef, I., Olson, D. L., Eberthart, M., and Edwards, G. R. 2002. Hydrogen trapping in ferritic steel weld metal. *International Materials Reviews* 47, pp. 191–223.

30. Hirth, J. P. 1980. Effects of hydrogen on the properties of iron and steel. *Metall. Mater. Trans.* A 11A, pp. 861–890.

31. Valentini, R., and Solina, A. 1994. Influence of microstructure on hydrogen embrittlement behaviour of 2.25Cr-1Mo steel. *Materials Science and Technology* 10, pp. 908–914.

32. Lee, K. Y., Lee, J. Y., and Kim, D. R. 1984. A study of hydrogen-trapping phenomena in AISI 5160 spring steel. *Mater. Sci. Eng.* 67, pp. 213–220.

33. Li, G. F., Wu, R. G., and Lei, T. C. 1992. Carbide/matrix interface mechanism of stress corrosion cracking behavior of high-strength CrMo steels. *Metall. Mater. Trans.* A 23A, pp. 2879–2885.

34. Sen, M., and Balasubramaniam, R. 2001. Hydrogen trapping at carbide-matrix interfaces in Fe_3Al-C intermetallics. *Scripta Materialia* 44, pp. 619–623.

35. Yoshino, Y. 1982. Low-alloy steels in hydrogen sulfide environment. *Corrosion* 38, pp. 156–167.

36. Regina, J. October 2005. PhD thesis, Lehigh University, Bethlehem, Pa.

37. HSC Chemistry for Windows. 4.0. 2002.